INVITED PAPER

Plasmonic Organic Hybrid Modulators—Scaling Highest Speed Photonics to the Microscale

This paper explores plasmonics as a viable technology for single-channel intensity modulators and more sophisticated IQ modulators.

By Christian Haffner, Wolfgang Heni, Yuriy Fedoryshyn, Arne Josten, Benedikt Baeuerle, Claudia Hoessbacher, Yannick Salamin, *Student Member IEEE*, Ueli Koch, Nikola Đorđević, Pol Mousel, Romain Bonjour, Alexandros Emboras, David Hillerkuss, Pascal Leuchtmann, Delwin L. Elder, Larry R. Dalton, *Senior Member IEEE*, Christian Hafner, and Juerg Leuthold, *Fellow IEEE*

ABSTRACT | Complementing plasmonic slot waveguides with highly nonlinear organic materials has rendered a new generation of ultracompact active nanophotonic components that are redefining the state of the art. In this paper, we review the fundamentals of this so-called plasmonic–organic-hybrid (POH) platform. Starting from simple phase shifters to the most compact *IQ* modulators, we introduce key devices of high-speed data communications. For instance, all-plasmonic Mach–Zehnder modulators (MZMs) are reviewed and long-term prospects are discussed. This kind of modulator already features unique properties such as a small footprint ($< 20\ \mu m^2$), a large electro-optic bandwidth (> 110 GHz), a small energy consumption ($\sim$25 fJ/b), a large extinction ratio (> 25 dB) in combination with a record small voltage-length product of 40 Vμm. Finally, as an example for seamless integration we introduce novel plasmonic *IQ* modulators. With such modulators we show the generation of advanced modulation formats (QPSK, 16-QAM) on footprints as small as 10 μm $\times$ 75 μm. This demonstration ultimately shows how plasmonics can be used to control both phase and amplitude of an optical carrier on the microscale with reasonably low losses.

KEYWORDS | *IQ* modulators; linear electro-optic effect; Mach–Zehnder modulators (MZMs); plasmonic modulators; plasmonic–organic-hybrid (POH); plasmonics

I. INTRODUCTION

Electro–optical modulators are key elements in optical communication systems, especially in long-haul systems. Mach–Zehnder modulators (MZMs) and nested Mach–Zehnder modulators (*IQ* modulators) based on $LiNbO_3$ have already shown the encoding of advanced modulation formats such as PDM-64QAM with line rates up to 1 Tb/s per modulator [1]. If assembled in a larger system, photonics ultimately offers Pb/s capacity [2]. In reality, such a Pb/s system would require several thousands of modulators; and while electronics are very compact, the large cm^2 footprint of $LiNbO_3$-based modulators would pose severe limitations to the overall footprint.

Manuscript received January 30, 2016; revised March 16, 2016; accepted March 21, 2016. Date of publication June 7, 2016; date of current version November 18, 2016. This work was supported in part by the National Science Foundation under Grant DMR-1303080; by the U.S. Air Force Office of Scientific Research under Grant FA9550-15-1-0319; and by the European Research Council (ERC) under the PLASILOR Grant (EU-670478). C. Haffner and W. Heni contributed equally to this work.

C. Haffner, **W. Heni**, **Y. Fedoryshyn**, **A. Josten**, **B. Baeuerle**, **C. Hoessbacher**, **Y. Salamin**, **U. Koch**, **N. Đorđević**, **P. Mousel**, **R. Bonjour**, **A. Emboras**, **D. Hillerkuss**, **P. Leuchtmann**, **C. Hafner**, and **J. Leuthold** are with the Institute of Electromagnetic Fields (IEF), ETH Zürich, 8092 Zürich, Switzerland (e-mail: haffnerc@ethz.ch).

D. L. Elder and **L. R. Dalton** are with the Department of Chemistry, University of Washington, Seattle, WA, 98195-1700 USA.

Digital Object Identifier: 10.1109/JPROC.2016.2547990

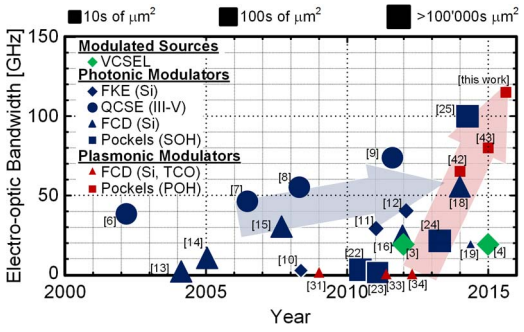

Fig. 1. ***Bandwidth and footprint of electro-optical integrated modulators (experimental results only). The plot shows the improvement of the bandwidth over the last 15 years for integrated photonic and plasmonic modulator as well as directly modulated VCSELs. The size of the symbol indicates the required footprint and the shape of the symbol indicates the effect it relays on. It can be seen that photonic modulators have experienced a steady but moderate increase in bandwidth over the years (blue arrow). The plot also shows how newer plasmonic modulators are about to outperform the photonic counterparts at a much smaller footprint (red arrow). The expected bandwidth is well beyond hundreds of gigahertz.***

To present the bigger picture, we have summarized the best in-class electro–optical bandwidths for various integrated optical technologies and configurations in Fig. 1. So, for instance, directly modulated vertical-cavity surface-emitting lasers (VCSELs) have emerged as a viable and compact ($> 1000\ \mu m^2$) solution for optical high-speed communications in data centers [3], [4]; see ◆ in Fig. 1. Unfortunately, they generate chirped signals [5]. A more versatile solution is provided by integrated external photonic modulators, which do not suffer from a strong chirp [5]. After a decade of development, external photonic modulators have made tremendous progress, for instance, in terms of electro–optic bandwidth, as indicated by the light blue arrow in Fig. 1 (note that larger symbols indicate larger footprint). These modulators encode electrical signals onto a continuous-wave (CW) optical carrier by utilizing various effects such as the quantum-confined Stark effect (QCSE: ●) in III-V semiconductors [6]–[9], the Franz–Keldysh effect (FKE: ◆) in silicon–germanium (SiGe) [10]–[12], free-carrier dispersion (FCD: ▲) effects in silicon [13]–[20], and the Pockels effect (■) in silicon–organic–hybrid (SOH) modulators [21]–[25]. Modulators based on these effects have been shown in resonant [19], [20], [23] as well as nonresonant configurations [6]–[18], [21], [22], [24], [25]. Resonant disc modulators feature high Q-factors enabling compact devices with footprints of $\approx 20\ \mu m^2$. However, a high Q-factor comes at the cost of a limited electro–optical bandwidth (≈20 GHz) [19]. Alternatively, nonresonant absorption modulators based on QCSE [6]–[9] or FKE [10]–[12] effects have demonstrated electro–optical bandwidths up to 74 GHz [9] with footprints of 40 μm^2 [11]. Yet, the capability of these devices to access multiple amplitude and phase levels in order to encode advanced modulation formats is limited. Conversely, these constraints can be overcome by MZM configurations [17], [24]. Several MZM-based devices have shown electro–optical bandwidths of 55 [18] and 100 GHz [25] when utilizing the FCD in Si and the Pockels effect in SOH, respectively. However, due to a relatively weak light–matter interaction in photonic structures, these devices require rather long phase shifters, typically $> 500\ \mu m$, to achieve sufficient phase shifts. As shown in Fig. 1, all modulators featuring large bandwidths are bulky devices with footprints way above several hundreds of squared micrometers [9], [18], [25]. Yet, ideally, electro–optic modulators should feature a compact footprint on the order of squared micrometers, a large bandwidth (> 100 GHz) with the least power consumption (∼fJ/b), and at the same time provide access to advanced modulation formats.

Plasmonics has been considered for some time to be a viable option for realization of compact and fast modulators [26]–[37]. In plasmonics, light is guided as a surface plasmon polariton (SPP) at metal–insulator interfaces [38]. This enables light confinement well below the diffraction limit resulting in an enhanced light–matter interaction at the cost of ohmic losses [39]–[41]. The losses are indeed a fundamental limit for long devices. Yet, the enhanced light–matter interaction allows to realize short devices and, in fact, can even overcompensate for the loss within certain limits. Indeed, several research groups have reported micrometer-sized plasmonic modulators mostly exploiting the FCD effect (▲); see Fig. 1 [31], [33], [34]. In the future, such modulators are also expected to outperform their photonic counterparts in terms of electro–optical bandwidth. High-speed operation, however, has only recently been demonstrated by modulators relying on the plasmonic–organic–hybrid (POH) platform (■) [42], [43]. From Fig. 1, one can recognize improvements that, even though relying on a new technology, already go beyond what photonics can offer. POH modulators have experienced a rapid evolution, starting with the first proof of principle in 2014 60-GHz high-speed phase modulator [42], followed by the first demonstrations of an all-plasmonic MZM in 2015 [43], which has then fostered the development of a remarkably compact plasmonic *IQ* modulator [44]. Meanwhile, plasmonic modulators [45]–[50] have been demonstrated to operate with multilevel signals [47] to directly convert millimeter waves to the optical domain [50], to switch at the atomic scale [49] and a plasmonic interconnect solution has been suggested [48].

In this paper, we review the POH platform, where plasmonic wave guiding is combined with organic second-order nonlinear optical (NLO) materials to enable ultrafast active devices. At the same time, we demonstrate the potential for scaling to more complex circuits

by introducing the first plasmonic *IQ* modulator. To put things in context, we give here the absolute numbers as obtained from the first generation of POH modulators. They feature:

- footprints of a few squared micrometers;
- encoding of advanced modulation formats such as QPSK and 16-QAM enabling 144 Gb/s;
- electro–optic bandwidths >110 GHz (≈THz expected);
- electrical energy consumption ≈ 25 fJ/b;
- voltage-length products of 40 Vμm;
- extinction ratios (ERs) > 25 dB;
- insertion losses (IL) of 5 dB for a single MZM.

The paper is organized as follows. In Section II, we review the different organic-based modulator technologies such as the conventional organic waveguide modulators, the SOH modulators, and the POH modulators. Section III discusses the physics behind the POH waveguide and the operating principle of the POH phase modulator. In Section IV, we discuss the all-plasmonic MZM. Section V reports on the performance of the first plasmonic *IQ* modulator. For more general reviews on plasmonics or on organic NLO materials in general, we recommend [51]–[53], respectively.

II. POH MODULATORS: LIGHT–MATTER INTERACTION BEYOND THE DIFFRACTION LIMIT

Merging NLO materials [52] with plasmonic structures [41] allows us to combine the advantages of each technology without suffering from the drawbacks of the respective individual technologies [42], [43]. We discuss the advantages of the POH technology over its two photonic predecessors with the help of Fig. 2. The figure depicts an artistic view of three generations of modulators that all utilize second-order NLO materials to encode an electrical signal onto an optical carrier. The three generations of modulators are: 1) an organic waveguide modulator [54]; 2) a photonic SOH modulator [55]; and 3) a POH modulator [42]. One can see that the size of the modulators decreases from centimeters, to millimeters, and finally to micrometers when going from left to right. To understand this evolution we first discuss the NLO material system and then discuss how its properties can be used to take full advantage of the nonlinear characteristics.

Organic NLO materials with a dominant linear electro–optic effect offer some unique advantages [56].

- Linear phase modulation: The linear electro–optic effect (Pockels effect) [57] allows one to linearly modulate the phase of an optical signal by means of an applied electrical field. An advantage of the linear electro–optic effect is that the optical absorption of the material is hardly affected by the phase modulation.
- Ultrafast speed: The linear electro–optical effect is a parametric light–matter interaction. As such, the process works on an attosecond timescale and the electro–optical bandwidth of the modulator is thus only limited by the resistor–capacitor (RC) time constant of the electrodes and its associated wires [52].
- Highest nonlinearities: The strength of the light–matter interaction is defined by the electro–optic coefficient (r). Current organic electro–optic (OEO) materials exhibit electric field poling-induced r coefficients up to approximately 400 pm/V [58]–[61], more than an order of magnitude larger than the electro–optic coefficients of $LiNbO_3$ ($r \approx 30$ pm/V).

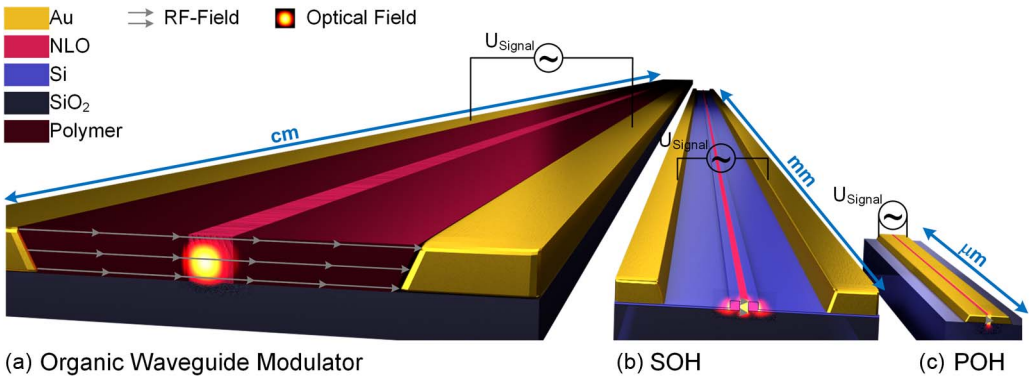

Fig. 2. ***Artistic view of different organic modulator technologies. (a) Organic waveguide modulators. Light (optical mode profile) is guided within a waveguide formed by the organic NLO material; the phase is modulated by the applied drive voltage U_{Signal} and drops off over the distance of a few micrometers as indicated by the radio-frequency (RF) field (gray). Such organic modulator devices have centimeter lengths. (b) SOH modulators have submillimeter lengths. Here, the electrical field drops only over the slot filled with the organic material. However, the performance is still limited as the diffraction limit forbids complete confinement of light to the slot. (c) This can be overcome by the POH approach, which is not diffraction limited and enables modulator lengths of only several micrometers.***

- Low energy consumption: The energy consumption in $\chi^{(2)}$ electro–optic modulators in an open-circuit configuration is mainly influenced by the capacitance. The capacity is proportional to the material's permittivity at radio frequencies ($\varepsilon_{\mathrm{GHz}}$) and the dimensions of the device. Organics feature a multiple times lower permittivity compared to inorganic electro–optic materials [56], and thus allows to operate the modulator with less energy.

These characteristics of the organic NLO materials can be exploited for electro–optic modulation. In the following, we will briefly discuss the three kinds of modulators.

A. Organic Waveguide Modulators

Organic waveguide modulators have already shown small signal sinusoidal modulation up to 150 GHz [54]. In these modulators, the waveguides are formed by the NLO material [Fig. 2(a)]. To apply the electrical drive voltage (U_{Signal}), the waveguides are embedded between two Au contact electrodes (yellow). By exploiting the Pockels effect, the refractive index of the waveguide (n_{mat}) is linearly changed in the presence of an electrical field

$$\Delta n_{\mathrm{mat}} = \frac{r}{2} \cdot n_{\mathrm{mat}}^3 \cdot E_{\mathrm{Signal}} = \frac{r}{2} \cdot n_{\mathrm{mat}}^3 \cdot \frac{U_{\mathrm{Signal}}}{d_{\mathrm{separation}}}. \quad (1)$$

Optical modes propagating in the waveguide experience a phase shift proportional to Δn_{mat}. In the case of a constant voltage, this effect is inversely proportional to the separation distance ($d_{\mathrm{separation}}$) of the two electrodes. Thus, a small gap between the electrodes would be desirable. However, the minimum separation is defined by the size of the mode, which is diffraction limited to a large mode because of the small refractive index difference between the guiding organic materials ($n_{\mathrm{mat}} \approx 1.6$–$1.8$) and the cladding/substrate materials ($n_{\mathrm{SiO2}} \approx 1.44$). This results in an electrode spacing of several micrometers, which due to the weak light–matter interaction leads to modulator lengths of centimeters [54]. For the sake of completeness, it should be mentioned here that typical implementations of the organic modulator would be along the vertical axis. However, to emphasize the evolution of the modulators and their operating principle, we have drawn the organic modulator in a lateral arrangement of the electrodes with the waveguide.

B. SOH Modulators

A more efficient approach to exploit the Pockels effect on the silicon platform is the SOH technology [55]. As shown in Fig. 2(b), conductive silicon (blue) is used to form two Si rails separated by a narrow slot, which is filled with the NLO material. The advantage of this approach is that the voltage drops off across the narrow slot of ~150–200-nm width. This way, the electrical field has its maximum in the narrow NLO slot. As the electrical field is much higher than in the organic waveguide modulator, the length of the modulator can be reduced to millimeters and submillimeters. Nevertheless, this configuration suffers from two main drawbacks. First, silicon as a semiconductor has a higher resistance than metals leading to a limited RC response [62]. Second, the optical mode is only partially confined to the NLO material so that only parts of the optical mode and the electrical field interact (the field interaction factor is in the order of 0.1 [43]). The limited interaction then strongly reduces the efficiency of the phase modulator.

C. POH Modulators

In contrast to the previous two approaches, POH modulators use the Au contact electrodes to directly form a metal–insulator–metal (MIM) slot waveguide [see Fig. 2(c)]. At the gold-NLO interfaces, light is guided as SPPs. This approach combines the many advantages offered by organic NLO materials with plasmonic slot waveguides, and allows one to mitigate the deficiencies of the previous technologies by taking advantage of plasmonics, namely:

- Subdiffraction confinement of light: Plasmonics offers light confinement in MIM waveguides well below the diffraction limit. SPPs are particularly well confined to the metal–insulator surface for low refractive index materials such as organic NLO materials [39], [41].
- Enhanced light–matter interaction: The achievable voltage–length product in plasmonics is one order of magnitude smaller compared to photonics. This can be traced back to an increased field energy interaction factor and a large slow down factor. The enhanced light–matter interaction is discussed in detail in Section III.
- Small RC time constants: Highly conductive metals are used to guide light and electrical signals simultaneously, i.e., $R \rightarrow 0$. In addition, taking advantage of the enhanced light–matter interaction devices are very short such that potential capacitances between the metals are sufficiently small, resulting altogether in subpicosecond RC time constants ($\tau_{\mathrm{RC}} <$ ps).
- Reduced plasmonic losses: Recent measurements of the optical properties of gold thin films [43], [63], [64] revealed that plasmonic losses of noble metals are lower compared to previously reported values by Johnson and Christy [65]; see Fig. 3. In addition, since the length of plasmonic devices is typically in the micrometer range, the total loss through the device is relatively low.

Thus, plasmonics provides a viable solution to overcome the drawbacks of purely organic or SOH approaches as light can be confined within low refractive index materials on the nanometer scale by utilizing MIM waveguides.

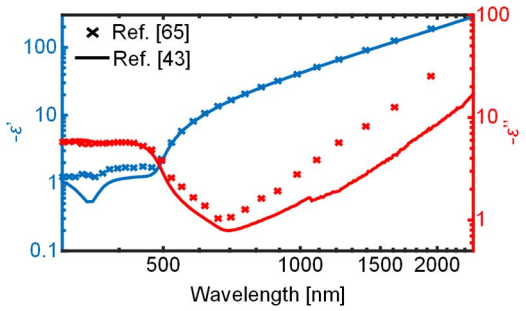

Fig. 3. *Real and imaginary permittivity values of Au: Progress in fabrication has led to a reduction of plasmonic losses in noble metals by as much as a factor 2. The real* (ε') *and imaginary* (ε'') *parts of the permittivity are plotted as a function of the wavelength. The curves show the newly measured values (solid lines) and the crosses show the standard values as reported in [65]. Image adapted from [43].*

III. POH WAVEGUIDES

This section starts with the optical properties of passive plasmonic slot waveguides before discussing their active electro–optic implementation in a POH phase modulator.

A. Passive MIM Waveguide

The longitudinal cross section of a passive MIM waveguide is depicted in Fig. 4(a). The waveguide is defined by two gold layers separated by w and a layer of insulating nonlinear material in between. SPPs propagate parallel to the metal–insulator interfaces as indicated by the direction of the wave vector β. Equivalent to photonics, SPPs can be described as plasmonic modes which are only TM polarized (only E_x, E_z, and H_y are unequal to zero) [66]. Following [41], we will discuss the properties of these modes where the MIM stack is assumed to be homogenous along y. Starting from the Helmholtz equation, the transverse magnetic (TM) field distribution within each layer m can be described by

$$\begin{aligned} H_{y,m}(x,z) &= \left(A_m e^{k_{x,m}\cdot x} + B_m e^{-k_{x,m}\cdot x}\right)e^{j\gamma z} \\ E_{z,m}(x,z) &= \left(-j\frac{k_{x,m}}{\omega\varepsilon_0\varepsilon_m}A_m e^{k_{x,m}\cdot x} + j\frac{k_{x,m}}{\omega\varepsilon_0\varepsilon_m}B_m e^{-k_{x,m}\cdot x}\right)e^{j\gamma z} \\ E_{x,m}(x,z) &= \left(\frac{\gamma}{\omega\varepsilon_0\varepsilon_m}A_m e^{k_{x,m}\cdot x} + \frac{\gamma}{\omega\varepsilon_0\varepsilon_m}B_m e^{-k_{x,m}\cdot x}\right)e^{j\gamma z} \end{aligned} \quad (2)$$

where γ is the complex propagation constant. Its real part β describes the phase propagation while its imaginary part α models the absorption. Here, a positive β corresponds to a forward propagating wave. The transverse wave vector $k_{x,m}$ is related to γ by $k_m^2 = \gamma^2 - k_0^2\varepsilon_m(\omega)$. The relative permittivity of the metal (M) and insulator (I) is given by ε_M and ε_I, respectively. The angular frequency is ω. A_m and B_m are constants associated with the respective layer m. Guided modes require that energy is confined to the core, meaning the field intensity must be zero for $x \to \pm\infty$. This requires A_1 and B_3 to be zero as k_x is larger than zero. Solving (2) for the tangential boundary conditions leads to the mode's dispersion relation $\beta(\omega)$, which is defined by the implicit equation

$$e^{-2k_1 w} = 2\frac{k_I/\varepsilon_I(\omega) + k_M/\varepsilon_M(\omega)}{k_I/\varepsilon_I(\omega) + k_M/\varepsilon_M(\omega)}. \quad (3)$$

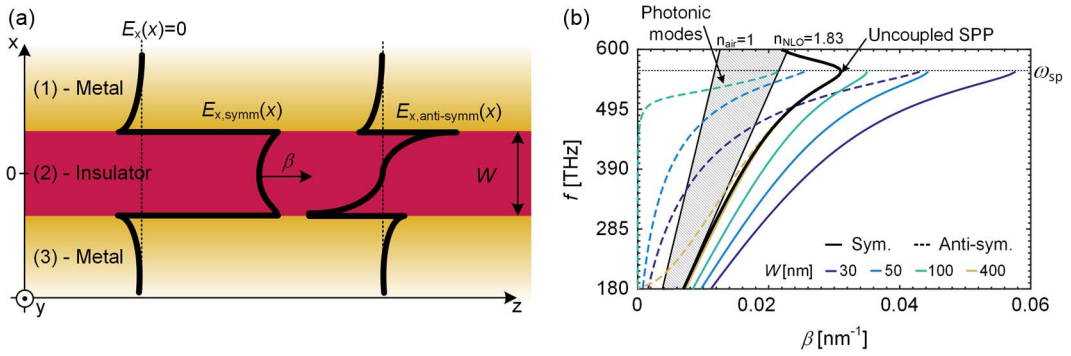

Fig. 4. *Properties of plasmonics modes. (a) MIM-stack homogenous along y-direction. Red indicates the insulating organic NLO material while yellow represents Au. The* E_x *field of the fundamental symmetric plasmonic mode is drawn in black. The field in the dielectric is quite enhanced over the field in the metal due to the large mismatch between NLO's and metal's permittivity. (b) Dispersion relation* $\beta(\omega)$ *for frequencies ranging from 180 to 600 THz for the symmetric (solid line) and antisymmetric (dashed) plasmonic modes at different slot widths. In the same plot, we also give the dispersion relation of an uncoupled SPP as it would exist at a single MI interface. The gray area highlights all possible wave vectors of a hypothetical ideal photonic waveguide with an air cladding and the NLO material as a guiding layer. Plasmonic modes are guided when their propagation constants* β *are larger than the NLO's light line. These modes are confined to the near field and cannot couple to photonic modes. The symmetric mode exists for all frequencies and widths while the antisymmetric mode is cut off for small frequencies and widths.*

Two orthogonal plasmonic solutions can be found for the slot waveguide [Fig. 4(a)]. One has a symmetric E_x component while the other one has an antisymmetric E_x component with respect to the center of the waveguide. When increasing the slot width, the left-hand side of (3) becomes zero and the right-hand side can be rearranged to the following equation when substituting $k_m^2 = \gamma^2 - k_0^2\varepsilon_m(\omega)$:

$$\gamma(\omega) = \beta_0(\omega)\sqrt{\frac{\varepsilon_{\mathrm{M}}(\omega)\varepsilon_{\mathrm{I}}(\omega)}{\varepsilon_{\mathrm{M}}(\omega)+\varepsilon_{\mathrm{I}}(\omega)}}. \tag{4}$$

This is the solution for a single metal–insulator interface. In the case of a large slot width, both modes converge toward the solution of single uncoupled SPPs.

Fig. 4(b) shows the frequency f ranging from 180 to 600 THz as a function of the propagation constant's real part β. The graph compares plasmonic symmetric (solid) and antisymmetric (dashed) modes, the plasmonic mode of a single interface (black), and all wave vectors which can exist in a photonic NLO waveguide (gray hatched area). The figure shows only symmetric and antisymmetric bound modes below the plasmon frequency ω_{SP}. It can be seen that the wave vector below the plasmon frequency of the uncoupled SPP mode is always larger than the wave vector of the organic NLO light line ($n_{\mathrm{NLO}} = 1.83$). Thus, once launched as an SPP, light cannot couple back to the photonic modes as it is confined to the interface. In the case of the coupled symmetric plasmonic mode, the wave vector β is larger for reduced slot widths, resulting from a stronger confinement to the near field; see (2). In contrast, the antisymmetric modes are in the cutoff, and guided modes exist only in the limit of large widths or high frequencies. Thus, plasmonic modulators with a narrow slot only guide the fundamental plasmonic modes. This mode shows a significant light confinement in combination with an enhanced transverse electrical field and a strong nonlinear dispersion relation.

B. POH Phase Modulator

Fig. 5(a) shows a colorized SEM image of a typical POH phase modulator (PPM) realized on an SOI substrate. Gold (Au) contact pads are used simultaneously to form the 150-nm high MIM (Au/NLO/Au) slot waveguide and to apply the electrical signal to the slot via highly conductive metallic contacts. The slot is filled with an organic second-order NLO material and the Pockels effect can be exploited to encode the electrical signal onto the optical carrier. Light is coupled to and from the MIM slot by silicon waveguides via photonic–plasmonic converters (PPCs) [67], which gradually convert the photonic mode into a plasmonic mode by tapering down the Si waveguides and tapering up the contact pads. The SPP then propagates along the slot. When a voltage is applied across the slot, the refractive index of the electro–optic organic material is changed and a phase shift is induced onto the SPP. The accumulated phase shift ($\Delta\varphi$) after a propagation length L is given by [43]

$$\begin{aligned}\Delta\varphi(L, E_{\mathrm{sig}}) &= \Delta\beta \cdot L = \frac{2\pi}{\lambda_0} \cdot \Delta n_{\mathrm{eff}}(E_{\mathrm{sig}}) \cdot L \\ &= \frac{2\pi}{\lambda_0} \cdot \Gamma \cdot n_{\mathrm{slow}} \cdot \frac{\Delta n_{\mathrm{mat}}(E_{\mathrm{sig}})}{n_{\mathrm{mat}}} \cdot L. \end{aligned} \tag{5}$$

The phase shift depends on the change of the effective refractive index Δn_{eff} of the plasmonic mode. Its strength depends on three factors, namely, the field energy interaction factor (Γ), the slow down factor of the SPP (n_{slow}), and the electric field induced relative change of the material's refractive index ($\Delta n_{\mathrm{mat}}/n_{\mathrm{mat}}$).

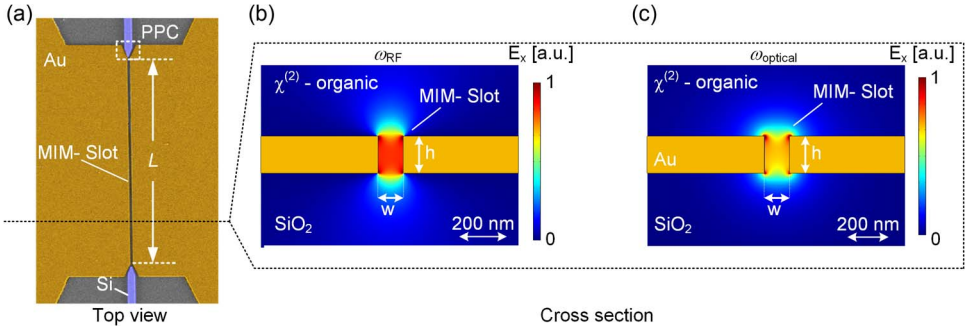

Fig. 5. ***Plasmonic phase modulator. (a) Colorized SEM image of the phase modulator. Au is indicated in yellow, silicon in blue, and SiO_2 is given in gray. The two Au contact pads form the MIM slot waveguide, which is filled with the organic material. Light is coupled to and from the slot by PPCs. The cross section with the RF and optical fields are shown in (b) and (c) for a slot with height (h) and slot width (w) of 150 and 100 nm, respectively. Both images show the simulated E_x component at optical frequency and RF, respectively. Their perfect overlap suggests the strongest possible light–matter interaction.***

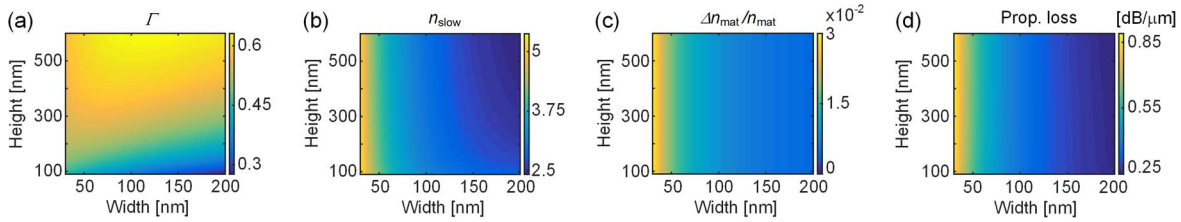

Fig. 6. ***Contributions to the enhanced light–matter interaction. The figures show the dependency of the three mayor terms that contribute to the overall refractive index change in a plasmonic modulator as a function of the slot width and slot height. In all plots, the applied voltage across the slot has been kept constant. (a) Field energy interaction factor. It is proportional to the overlap integral between RF and optical field. (b) Slow down factor. (c) Dependency of the relative change of the refractive index. It varies inversely with the width of the slot. (d) Plasmonic propagation losses as a function of the slot geometry.***

In the following, we will briefly discuss these three dominant factors and the plasmonic propagation losses as a function of the waveguide geometry (height and width) [Fig. 6(a)–(d)]. For more details as well as for a comparison with the SOH approach we refer the reader to [43].

The field energy interaction factor Γ is largest when the field profile at optical frequencies and RFs overlap the most [43]. The simulated E_x components of the RF field and the optical field are shown in Fig. 5(b) and (c), respectively, for a slot width w of 100 nm and a height h of 150 nm. Only the E_x component of the field in the slot's active region $(w_{slot} \cdot h_{slot})$ is contributing to the light–matter interaction [43]. While both fields are mostly confined to the slot, the fields are leaking out in vertical direction, thereby reducing Γ. Fig. 6(a) shows Γ as a function of slot width and height, based on (22). Smaller width or larger height results in an enhanced field energy interaction factor as the leakage of the optical field in the vertical direction decreases. Upon a further decrease of the width w, below 30 nm, the field energy interaction factor will decrease as the field penetrates into the metal.

A large slowdown factor (n_{slow}) is of benefit as a slowed SPP has more time to interact with matter. It originates from the field penetration into the metal. This can be understood by the fact that the fraction of the electric field in the metal has an E_x field in the opposite direction; see Fig. 4(a). The direction of the H_y field is the same in the metal and the insulator; see (2). As a consequence, the fraction of the mode in the metal has a pointing vector showing in the backward direction. Thus, the SPP is on average slowed down when the field penetrates more into the metal. The quantitative results for n_{slow} are shown in Fig. 6(b) as a function of w and h. For smaller widths, the increase of the slowdown factor shows that the penetration of the field into the metal is increasing with narrower slots ($n_{slow} = 2.6$ at 200 nm and up to 4.9 at 30 nm). Alternatively, the slowdown factor can be approximated by the slope of the dispersion relation—flat regions correspond to slower light; see Fig. 4(b).

Fig. 6(c) shows the change of the relative refractive index $\Delta n_{mat}/n_{mat}$ as a function of w and h for a constant voltage (3 V). The $1/w$ dependency of $\Delta n_{mat}/n_{mat}$ is due to the fact that the applied voltage drops completely across the nanometer-scaled MIM slot; see Fig. 5(b). This narrow slot is actually one of the reasons that the electrical fields are several orders of magnitude larger compared to organic waveguide modulators where the voltage drops over several micrometers.

The dependency of plasmonic propagation losses on the waveguide geometry is given in Fig. 6(d). The losses are highest for smallest w, as the field penetration into the metal is largest.

To evaluate the performance of PPMs we use a figure-of-merit (FoM) relating phase modulation per voltage and losses

$$\mathrm{FOM} = \frac{\Delta\varphi}{\text{propagation losses}_{\mathrm{dB}} \cdot U_{\mathrm{Sig}}} \left[\frac{\mathrm{rad}}{\mu\mathrm{m}} \cdot \frac{\mu\mathrm{m}}{\mathrm{dB}} \cdot \frac{1}{\mathrm{V}}\right]. \quad (6)$$

Here $\Delta\varphi$ is the accumulated phase change in radians after an SPP has propagated 1 μm divided by the propagation losses and an applied voltage U_{Signal}. Fig. 7 shows the simulated FoM as a function of the slot width and height for an elecro-otpic coefficient r_{33} =180 pm/V. The figure shows that a decreasing slot width, i.e., enhancing the interaction, is providing a larger FoM, despite the increased propagation losses. This means that the enhanced nonlinearity overcompensates for the propagation losses and that total device losses can be reduced when downscaling the slot width [43], [47]. The dashed line indicates the limits of our fabrication technology in terms of height-to-width aspect ratios. In our process, aspect ratios of up to 3:1 can be fabricated reliably resulting in a maximum FoM of 0.095 for a slot width of 30 nm and height of 90 nm. A 4-μm-long MZM with such PPMs would require a voltages of ≈4.5 V to switch from on to off while having insertion losses of ≈4 dB leading to $U_\pi L$ below 20 Vμm.

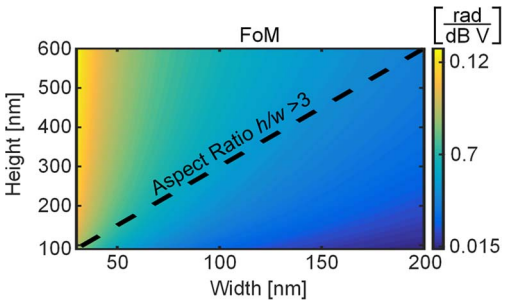

Fig. 7. *Figure of merit. The plot shows the achievable FoM as a function of the slot's height and width. The FoM shows how much phase shift can be accumulated per 1-dB propagation loss and 1-V applied voltage. The dashed line indicates an aspect ratio (h/w) of 3. This line marks the current fabrication limits. Aspect ratios above 3, even though more promising, are difficult to fabricate.*

Additionally, introducing most recent organic NLO materials with higher nonlinearities [58]–[61] would reduce the voltage length product below 10 Vμm and sub-fJ/b energy consumptions could be reached.

In our own experiments, we measured record voltage-length products down to 40 Vμm for a 6-μm-long MZM with slot widths of 40 nm. The discrepancy to the theory is attributed to the not yet optimized poling procedures and tilted sidewalls, which degrade the efficiency quite a bit for such narrow slots.

IV. INTEGRATED ALL-PLASMONIC MACH–ZEHNDER MODULATOR

Integrating two phase modulators into a plasmonic interferometer configuration allows one to fabricate Mach–Zehnder modulators, which are orders of magnitude smaller than any other MZM. Despite the exceptionally compact solution with a footprint of a few micrometers squared only efficient amplitude modulation up to highest speed is found. The operation principle, design guidelines, performance characteristics, and experimental results are discussed in the following sections by partially referring to results reported in [43] and by introducing more recent results.

A. Operating Principle

An all-plasmonic MZM (device A, Table 1) is shown in Fig. 8(a). The colorized SEM image shows the so-called "island" structure with suspended bridges that connect the "island" to the neighboring signal pad. The signal pad is used to contact the modulator using standard RF probes. Compared to other approaches [47], the island is a significantly narrowed signal electrode that allows the amplitude modulation to take place within the dimensions of a silicon photonic single mode waveguide.

Table 1 Device Parameters of the Various Modulators

DEVICE [REF.]	w_1 [nm]	w_2 [nm]	l [μm]	h_{Au} [nm]	TYPE
A **[43]**	90	100	5	200	MZM
B	40	45	6	150	MZM
C **[44]**	35	40	12	150	IQ
D **[44]**	80	90	8	150	IQ
E **[44]**	80	90	12	150	IQ

Silicon waveguides were used to feed CW light to the modulator and extract the modulated optical signal. To convert light from photonic into plasmonic modes photonic–plasmonic interference (PPI) sections are used at the input and output of the modulator section.

The operating scheme of the all-plasmonic MZM can be understood with the help of Fig. 8(b), showing the simulated E_x component in the off-state and the on-state of the modulator. Light guided in the input silicon waveguide (TE_{00}) is coupled to a symmetric plasmonic mode by tapering down the silicon waveguide. This symmetric plasmonic mode equally excites two in-phase SPPs in the upper and lower MIM slot waveguides. The two MIM waveguides are filled with a second-order NLO material (DLD164) [61] and represent the phase modulators of the device. The relative phase of the SPPs at the output of the phase shifters is actively controlled by a voltage (U_{Signal}) applied between the "island" and the outer ground electrodes. In the off-state, the voltage is chosen such that the phase difference between both arms is π and an antisymmetric plasmonic mode is excited at the output tip of the island. On the other hand, in the on-state, the SPPs of the two PPM are in phase and a symmetric plasmonic mode is excited at the outlet. The latter couples to a guided photonic mode (TE_{00}) of the silicon waveguide while the former is mainly coupled to lossy evanescent modes. Thus, the phase modulation is translated into an amplitude modulation.

B. Transfer Function of an All-Plasmonic MZM

The measured voltage-dependent intensity transfer function of device B (all-plasmonic MZM) is depicted in Fig. 9. This device features slot widths of ~40 nm and a length of 6 μm. Narrowing down the slot widths has been made possible by reducing the gold height from 200 nm (device A) to 150 nm. The applied direct current (dc) voltage was swept from −5 to +5 V while the transmitted optical power was measured. The measured power was normalized to the power in the on-state. The device is switched from the on-state to the off-state by a voltage of $U_\pi \approx 7$ V. Considering the μm-length of the device a record low voltage-length product of ≈40 Vμm was achieved. Furthermore, the measured ER between the on-state and the off-state is 26 dB which is significantly larger than the value reported in [43].

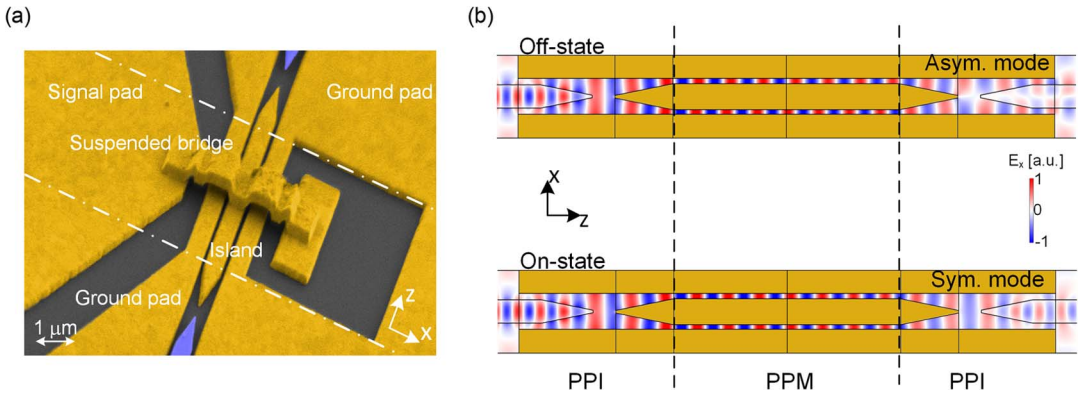

Fig. 8. ***The all-plasmonic MZM. (a) Colorized SEM image of the modulator. The plasmonic interferometer is formed by the metallic island and the metallic contact pads. An electrical signal can be applied to the island via a suspended bridge. Light is coupled to and from the interferometer by PPI. (b) FEM simulations showing the plasmonic modes in the off-state and the on-state. In the off-state, the fields are out of phase at the output, while they are in phase in the on-state. Light is coupled to guided modes of the silicon waveguide only when the modulator is in the on-state. Figure adapted from [43].***

The transfer function of the all-plasmonic modulator can be modeled by using transfer matrices adapted from [47]

$$\left[E_{\mathrm{TE}_{00},\mathrm{out}}\right] = T_{\mathrm{MZM}} \cdot \left[E_{\mathrm{TE}_{00},\mathrm{in}}\right] \tag{7}$$

with

$$T_{\mathrm{MZM}} = T_{\mathrm{PPI,out}} \cdot T_{\mathrm{PPM}} \cdot T_{\mathrm{PPI,in}}. \tag{8}$$

The incident photonic TE_{00} mode $(E_{\mathrm{TE}_{00},\mathrm{in}})$ is mapped onto the output TE_{00} photonic mode $(E_{\mathrm{TE}_{00},\mathrm{out}})$ of the silicon waveguide by the MZM's transfer matrix (T_{MZM}). The contributions of the individual components, such as PPIs and PPM, are given by their individual transfer matrices T_{PPI} and T_{PPM}, respectively

$$T_{\mathrm{PPI,out}} = \sqrt{c_{\mathrm{PPI,out}}} \cdot \left[\sqrt{r}\ \sqrt{1-r}\right] \tag{9}$$

$$T_{\mathrm{PPM}} = \begin{bmatrix} e^{-j\left(\beta_1+\Delta\beta_1(U_{\mathrm{Sig}})\right)L-\frac{\alpha_1}{2}L} & 0 \\ 0 & e^{-j\left(\beta_2+\Delta\beta_2(U_{\mathrm{Sig}})\right)L-\frac{\alpha_2}{2}L} \end{bmatrix} \tag{10}$$

$$T_{\mathrm{PPI,in}} = \sqrt{c_{\mathrm{PPI,in}}} \cdot \begin{bmatrix} \sqrt{r} \\ \sqrt{1-r} \end{bmatrix}. \tag{11}$$

The coupling efficiency of the PPI section is given by c_{PPI} while r represents the splitting ratio of the PPI coupler. A value of $r = 0.5$ indicates an equal splitting and combining of energy entering the PPM and leaving the PPM, respectively. T_{PPM} describes the evolution of the phase and amplitude along the two arms of the interferometer. The SPPs' propagation constant $\beta_i(w_i)$ as well as the SPPs' power attenuation $\alpha_i(w_i)$ depends on the geometry w_i of the waveguide. The modulation of the optical carrier by an applied electrical signal is described by $\Delta\beta_i(w_i, U_{\mathrm{signal}})$ which is a function of the applied voltage (U_{signal}) and slot width (w_i); see (5).

Data transmissions based on direct detection or coherent detection requires that the MZM be operated in the quadrature point (QP) or the Null point (NP; off-state), respectively. To operate this device in the respective operation point a phase offset in the two arms needs to be adapted to either $\pi/2$ for the QP or π for the NP operation. This can be achieved by either applying a voltage at the expense of higher electrical fields in the slots or by introducing asymmetric slot widths w_1 and w_2 in the phase shifter arms [43]. The latter approach also

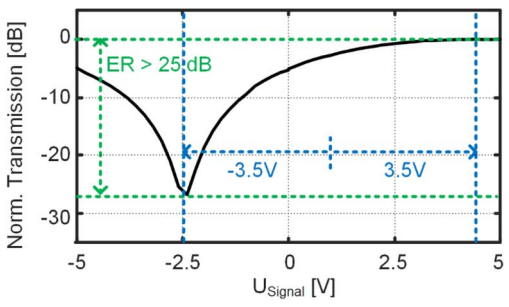

Fig. 9. ***Measured MZM transfer function. Normalized transmission plotted as a function of the drive voltage*** (U_{signal}) ***for phase shifters of 6-µm length. The measurement reveals record low voltage-length product of 40 V µm. The large ER confirms that the small footprint enables symmetric interferometers.***

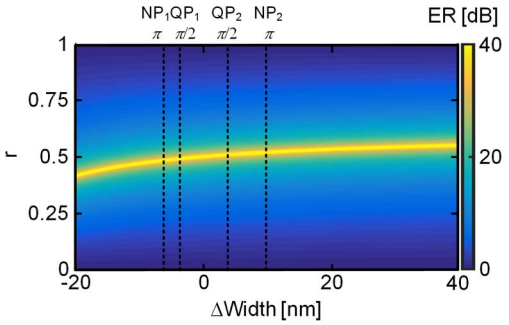

Fig. 10. *ER as a function of the splitting ratio r and a slot asymmetry. The dashed lines indicate slot width differences resulting in a phase difference between the two Mach–Zehnder arms in the amount of π and $\pi/2$. This phase differences correspond to operations in the NP and QP, respectively. The inherent reduction of the ER for unequal slot widths in these operation points is uncritical since the ER remains high in all cases. Only for large slot width differences the splitting ratio r has to be adapted to maintain high ERs.*

comes with an absorption $\Delta\alpha = \alpha_1 - \alpha_2$ change and thus influences the ER [47]. The general expression for the ER can be obtained by dividing the transfer function (10) for a signal in the on-state and the off-state. When uneven splitting ratios (11) are used in (10), then the ER can be derived as a function of the power splitting ratio r and slot width difference $\Delta w = w_1 - w_2$

$$\begin{aligned} \mathrm{ER}(\Delta w, r) &= \left|\frac{E_{\mathrm{on}}}{E_{\mathrm{off}}}\right|^2 \\ &= \left|\frac{re^{-\frac{\alpha_1(w_1)}{2}L} - (1-r)e^{-\frac{\alpha_2(w_2)}{2}L}}{re^{-\frac{\alpha_1(w_1)}{2}L} + (1-r)e^{-\frac{\alpha_2(w_2)}{2}L}}\right|^2 \\ &= \left|\frac{\left(e^{-\frac{\Delta\alpha(\Delta w)}{2}L}+1\right)r - 1}{\left(e^{-\frac{\Delta\alpha(\Delta w)}{2}L}-1\right)r + 1}\right|^2. \end{aligned} \tag{12}$$

The ER in (12) has been plotted in Fig. 10 as a function of slot width variations Δw, and a variation in the splitting ratio r for device B with a slot width of 40 nm, a gold height of 150 nm, and a device length of 6 μm. Since varying slot widths also results in phase offsets, we have indicated the respective phase offsets that correspond to a particular Δw by dashed lines. The yellow colors indicate that the ER remains high even when varying Δw. Furthermore, highest ERs can be achieved by adjusting the splitting ratio r and coupling more power to and from the MZI arm with higher propagation losses. It should be noted that a variation to a narrower slot in one arm increases the insertion loss of the device, while a variation to a wider slot increases the π-voltage U_π of the modulator [47]. Fabrication deviations can lead to a slight shift of the operation point, which can be adjusted by a small bias.

C. Losses

Of particular interest are the minimum inherent losses that go along with a plasmonic modulator. Using a new design, simulations indicated that total chip losses of a device can be as small as 4.5 dB. This would correspond to a loss reduction by 3.5 dB compared to the experimental losses reported for device A in [43]. The improvement results from an optimized photonic–plasmonic converter/splitter (PPI) structure. We will now discuss the losses in more detail.

Using (7), the losses for a symmetric MZM ($r = 0.5$ and $\alpha_1 = \alpha_2 = \alpha$) are

$$\begin{aligned} IL &= \left|\frac{E_{\mathrm{on}}}{E_{\mathrm{in}}}\right| = c_{\mathrm{PPI}}^2 \cdot \left|r \cdot e^{-\frac{\alpha_1}{2}L} + (1-r)\cdot e^{-\frac{\alpha_2}{2}L}\right|^2 \\ &= c_{\mathrm{PPI}}^2 e^{-\frac{\alpha}{2}L} \end{aligned} \tag{13}$$

where c_{PPI} accounts for the losses of the photonic-to-plasmonic converter and $\exp(\alpha/2 \cdot l)$ models the plasmonic propagation losses in the phase modulators.

With our first generation of PPI couplers, we found coupling losses of $c_{\mathrm{PPI}} = 2.75$ dB per coupler [43]. The first-generation geometry is shown in Fig. 11(a). The left image shows a top view with the simulated field profile while the right image depicts the structure at the position of the dashed line. Our analysis shows that the coupling efficiency for this geometry is strongly influenced by the height of the NLO cladding (h_{NLO}). The dependency of the coupling efficiency (red line) on the height of the NLO material is plotted in Fig. 11(c). Reducing the height enables coupling losses down to 1.1 dB while coupling losses on the order of 3 dB are found for NLO heights of 600–800 nm such as used in [43]. The large coupling losses are caused by radiative cladding modes in the NLO material, which are excited when light is coupled from the Si waveguide to SPPs in the broad MIM waveguide [Fig. 11(a) dashed line]. The radiative modes exist for large heights of the NLO material while they are cut off for small heights. Alternatively, the coupling efficiency can be improved by guiding light within Si rails up to the narrow phase shifter slots, as shown in Fig. 11(b). Thus, radiative modes are not excited and coupling losses below 1 dB can be achieved even for cladding heights of 800 nm; see Fig. 11(c), black line. This new geometry is now used for the plasmonic *IQ* modulators, as discussed Section V.

D. RF Performance

In order to demonstrate the high-speed capabilities of the plasmonic MZM, the electro–optical frequency response of the device was measured. Here, we show

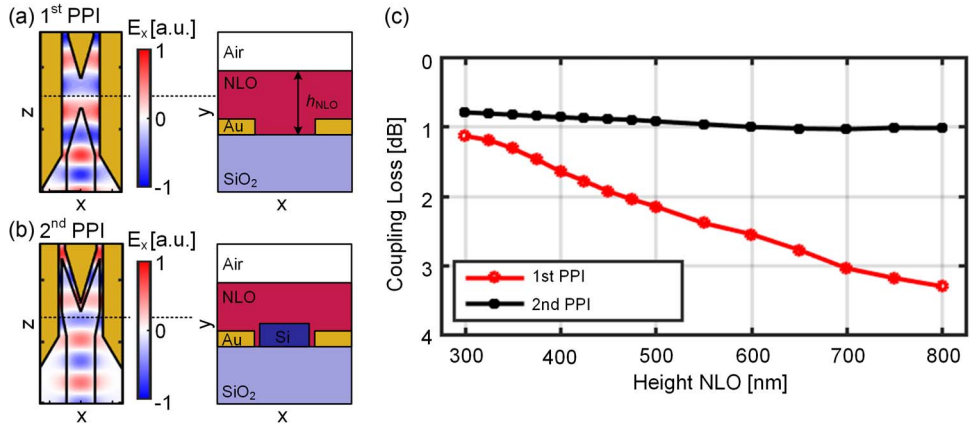

Fig. 11. ***Coupling schema for conversion of light from a silicon waveguide to a slot SPP. (a) Geometry of the coupler used in the initial proof of principle demonstration [43]. (b) Geometry of the improved coupling scheme as introduced here and more recently in [44]. The blue/red fields show simulated field distributions. (c) Coupling losses as a function of the cladding height. The coupling efficiency of the old design in (a) strongly varies with the cladding height, while the new scheme from (b) is almost independent of the cladding height with coupling losses below 1 dB.***

record 3-dB bandwidths exceeding 110 GHz for plasmonic modulators; see Fig. 12. In order to measure the frequency range from 75 to 110 GHz, a special millimeter-wave source and a probe were used. Two separate measurements of the same device have been performed. In the first experiment, the lower frequency range (15–70 GHz) was tested using the same setup as in previous demonstrations [43], [47], [68]. For the higher frequency range, an RF signal was fed into an amplifier combined with a Schottky diode producing multiple harmonics of the input signal. The undesired lower frequency signals were bandpass filtered by the output hollow waveguide. This way higher harmonic frequencies from 75 to 110 GHz were generated. A flat frequency response up to 110 GHz is found and it can be expected that the 3-dB bandwidth is much higher. Both measurements are normalized to the value measured at the lowest frequency. In order to estimate the maximum frequency response we can resort to an equivalent circuit analysis. We may assume that the device is RC limited [43]. When neglecting the contact pads and the internal resistivity of the driving source we are left with a device capacitance of 5 fF. Furthermore, we have a modulator resistivity of 0.36 Ω indicating a theoretical bandwidth up to 80 THz having a rise time of a few femtoseconds. In other words, such plasmonic modulators have frequency responses that go way beyond of what is currently needed.

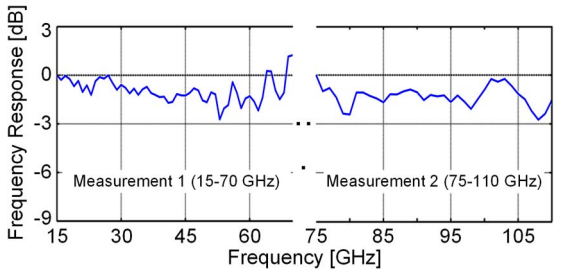

Fig. 12. ***High-speed RF-measurement electro-optic frequency response of an all-plasmonic MZM. Two separate measurements were performed for the lower (15–70 GHz) and higher frequency (75–110 GHz) range. Each measurement was normalized to its starting frequency at 15 and 75 GHz, respectively. No bandwidth limitation can be observed beyond the measurement range of 110 GHz.***

E. Data Transmission Experiments and Energy Consumption

The all-plasmonic modulator's capability to encode data at symbol rates up to 72 GBd was demonstrated by performing data generation experiments. Fig. 13 depicts a schematic of the measurement setup and the measured eye and constellation diagrams of the received signal including measured bit error ratios (BERs). Light from an external laser ($\lambda \approx 1534$ nm) was coupled to and from the chip using fully etched grating couplers. The modulated light was amplified before it was detected by a coherent receiver. In the receiver, standard DSP and postequalization was applied to mitigate the influence of the limited electrical bandwidth of our RF components. To modulate the light, an electrical data stream (PRBS $2^{15} - 1$) was generated by an arbitrary waveform generator (AWG). The electrical signal was amplified and fed to the modulator using GSG RF probes. In the first experiment, we investigated the performance at a data rate of 54 Gb/s using a square-root-raised cosine (SRRC) pulse shape (rolloff: $\alpha = 0.25$). The measured BER at 54 Gb/s was 7.3×10^{-5}. At 72 Gb/s, the BER has

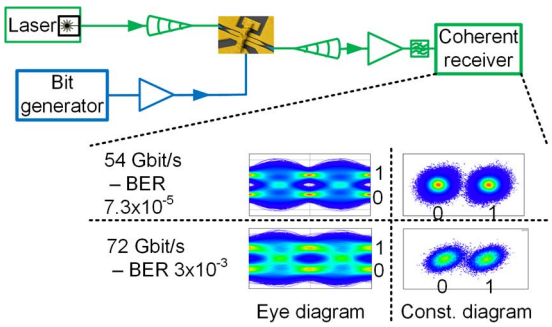

Fig. 13. *MZM high-speed data transmission experiment. Laser light (green) is coupled to and from the chip by grating couplers, amplified and received coherently. The electrical signal (blue) generated by a bit generator is encoded by means of the modulator onto the optical carrier. The received eye diagram and constellation diagrams are shown at the bottom. The BERs found with this device allow for high-speed data transmission up to 72 Gb/s when utilizing hard decision forward error correction. Figure adapted from [43].*

increased to 3×10^{-3}, which is still below the HD–FEC limit requiring a 7% overhead [69].

An energy consumption of ~25 fJ/b was derived for a drive voltage of 6 V_{pp} and an in-device capacitance of only 2.8 fF. The in-device capacitance was determined by 3-D simulations (CST Microwave Studio) using the geometries as found from SEM images of the fabricated device A.

V. INTEGRATED PLASMONIC *IQ* MODULATOR

The above mentioned all-plasmonic MZM is an essential building block for highly integrated nanophotonic circuits. Besides offering the benefits of a small footprint it also offers seamless integration capabilities with multiple plasmonic devices. As an example for highest integration, we introduce a plasmonic *IQ* modulator. We obtain a 1300-fold reduction in area compared to state-of-the-art semiconductor *IQ* modulators [70]–[72] by merging two plasmonic Mach–Zehnder modulators into an *IQ* modulator on a footprint of 10 μm × 75 μm [44]. In the following, we introduce the design of the plasmonic *IQ* modulator together with its operation principle. We then show its performance as well as data transmission beyond 100 Gb/s.

A. Device Design and Operation Principle

The plasmonic *IQ* modulator consists of two all-plasmonic MZMs in the arms of an outer MZM; see Fig. 14. Light from the left silicon single mode waveguide is fed into a 2 × 2 MMI (with only one input waveguide but two output waveguides). The 2 × 2 MMI splits an input carrier equally onto two outputs while introducing a relative phase delay of $\Delta\varphi = \pi/2$ between them. The in-phase (I) and quadrature (Q) components of the carrier are then fed onto two all-plasmonic MZMs, which are independently modulated by two electrical signals applied via pads S_Q and S_I, respectively. Modulated light from the two modulators is then combined by a symmetric 2 × 1 MMI and is coupled to an output silicon single mode waveguide.

The integrated MZMs share a common ground electrode (G_{IQ}) acting as an electrical shield, and thus, suppressing electrical crosstalk between in-phase and quadrature component. The signal electrodes (S_I and S_Q) of the two MZMs and the common ground electrode are contacted by suspended bridges. The outer ground electrodes (G_I and G_Q) of the modulators have been implemented as Au strips of 300-nm width.

B. Device Performance

The RF bandwidth of the *IQ* modulators has been characterized for up to 70 GHz and found to be flat. We

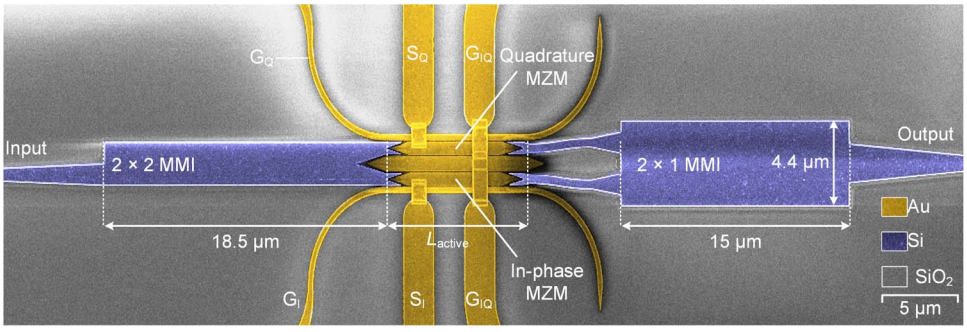

Fig. 14. *Colorized SEM image of a plasmonic IQ modulator comprising two seamlessly integrated MZMs embedded between two MMIs. Light fed from the left input waveguide is equally split by the 2 × 2 MMI and mapped with a 90° offset onto the upper and lower plasmonic MZMs. Information is encoded onto the optical carrier by means of the I and Q MZMs, which are connected via suspended bridges with the two electrical data signals (S_Q and S_I). Finally, the two signals from the modulators are combined to a complex optical signal by the subsequent 2 × 1 MMI. Figure adapted from [44].*

expect it to be flat up to 110 GHz and beyond, similar to the MZM; see Section IV-D.

Next, the device has been tested for electrical crosstalk between the in-phase and quadrature-phase MZMs. The electrical crosstalk was found to be smaller than −34.5 dB. The measurement was performed by applying a sinusoidal RF signals (10 GHz $\leq f_{RF} \leq$ 50 GHz) to one modulator and measuring the electrical signal on the other modulator using an electrical spectrum analyzer (ESA). The good suppression of crosstalk is probably due to the common ground electrode (G_{IQ}) and the small electrode length.

In the next step, we investigated the insertion losses of the *IQ* modulators. They were found to be 13.5 dB. To distinguish contributions of the individual components, we used test structures on the same chip. The 1 × 2 MMI contributes with 3.5 dB and the PPIs with 1.5 dB per converter. Another 7 dB are attributed to the 12-μm-long and 85-nm-wide plasmonic slot waveguides. This corresponds to plasmonic propagation losses of 0.58 dB/μm, which are higher than in previous batches and are related to variations in the fabrication process [43], [47]. Based on our previous experiments, we expect to be able to reduce propagation losses by 1.8 dB.

C. Data Experiment

To evaluate the performance of the plasmonic *IQ* modulator high-speed data transmission experiments were performed. The modulator was used to encode complex modulation formats onto an optical carrier. Encoding a quadrature phase-shift keying (QPSK) signal at a symbol rate of 72 GBd resulted in line rates of 144 Gb/s. Operation at higher modulation formats like 16-quadrature amplitude modulation (16-QAM) were demonstrated at 18 GBd; see the constellation diagrams in Fig. 15.

The data transmission experiments were performed using an external laser source (1535 nm $\leq \lambda \leq$ 1550 nm). Light was coupled to and from the chip using standard silicon grating couplers. The modulated signal was preamplified before it was received by a coherent homodyne detector. The electrical in-phase and quadrature-phase components were generated by two synchronized AWGs and were amplified to $\pm$2.5 V_p as measured at 50 Ω. The unterminated device gives an advantage of a factor of two, so that we expect $\pm$5 V_p across the modulators [47]. The electrical signals were applied using two electrical GSG RF probes. To adjust the operating points of the modulators, a dc bias of up to $\pm$6 V was applied.

The devices were tested for modulation performance at symbol rates from 18 to 56 GBd using an SRRC pulse shape (rolloff: $\alpha = 1$ to 0.28) and at 72 GBd using a rectangular pulse shape with a 2^{11}-bit-long De Bruijn sequence. In all experiments, standard DSP, predistortion, and postequalization were applied to compensate for the limited performance of the electrical components.

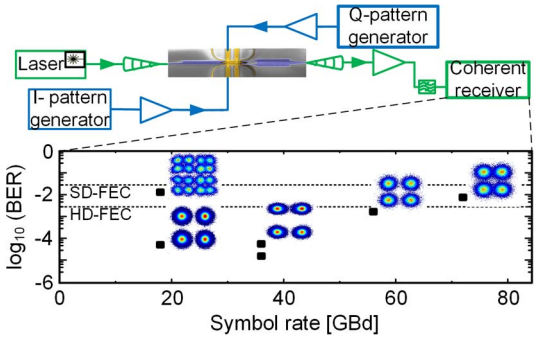

Fig. 15. ***IQ high-speed data transmission experiment. Laser light (green) is coupled to and from the chip by means of grating couplers, amplified and received coherently. The in- and quadrature phase components of the IQ modulator are encoded by electrical waveform generators (blue). The black squares indicate the received BERs at some specific symbol rates. The corresponding constellation diagrams are plotted next to the squares. BERs are below HD–FEC for symbol rates up to 54 GBd and below SD–FEC for QPSK at 72 GBd and 16-QAM 18 GBd resulting in line rates of 144 Gb/s. Figure adapted from [44].***

To verify the device performance in the high-speed data transmission experiments, we measured the BER of the received signals. Fig. 15 visualizes the measured BERs for different symbol rates and modulation formats. To show the signal quality, the corresponding constellation diagrams are inserted next to the data points. Devices C and D were used for the QPSK experiments while device E was used for the 16-QAM experiments; Table 1. For signals up to 56-GBd QPSK corresponding to a line rate of 112 Gb/s, the error ratios are well below the HD–FEC limit (7% overhead) of 2×10^{-3} [69]. At 72-GBd QPSK and 18-GBd 16-QAM, the measured BERs are 7.5×10^{-3} and 1.3×10^{-2}, respectively, and are below the SD–FEC limit of 2×10^{-2}, considering an overhead of 20% [73].

D. Energy Consumption

The plasmonic *IQ* modulator features an energy consumption of 27 fJ/b with the 16-QAM modulation format. This low energy consumption is a result of the high nonlinear interaction in the plasmonic slot; see Section II. The large nonlinear interaction results in reasonable drive voltages and very short devices. As a result of the short length the device capacitances are small leading to a low energy consumption.

In this section, we investigate the energy consumption of the plasmonic *IQ* modulator for *M*-QAM modulation formats, i.e., QPSK and 16-QAM in the case of an unterminated device [74]. Advanced modulation formats encode $\log_2(M)$ bits per symbols. Using the probability of a modulation format to switch from one state (amplitude level) to another, we derive a general expression for

the energy consumption per bit of our *IQ* modulator when encoding an *M*-QAM modulation format.

First, we note that the *IQ* modulator is driven independently by two MZMs, so that the total energy consumption per bit is obtained as a sum of the two modulators' switching energy

$$W_{IQ} = W_{I,\mathrm{MZM}} + W_{Q,\mathrm{MZM}}. \tag{14}$$

Thus, in the case of symmetric operation where both individual MZMs are driven with an identical voltage, we can reduce the discussion to the energy consumption of only one modulator.

Second, we operate the all-plasmonic MZMs unterminated (capacitive) so that hardly any current is flowing across the NLO material which is acting as an insulator. Thus, the dissipated switching energy for changing the voltage (U_{pp}) of the MZM's capacitor (C_{MZM}) is given by [75]

$$W_{\mathrm{switch,MZM}} = \frac{1}{2} U_{\mathrm{switch}}^2 C_{\mathrm{MZM}}. \tag{15}$$

In general, both *I* and *Q* signals have $M_{\mathrm{PAM}} = \mathrm{sqrt}(M)$ states. These states are equally separated by voltage steps of $U_{\mathrm{pp}}/(\mathrm{sqrt}(M)-1)$, where U_{pp} is the peak-to-peak voltage of the signal. The probability to be in a certain state A and to switch to another state B is equally distributed and given by

$$p_{A\to B} = \frac{1}{\left(\log_2(M)\right)^2}. \tag{16}$$

Based on this we can derive the total energy consumption for a transition from any symbol *A* to any symbol *B* by

$$W_{\mathrm{MZM,Symbol}} = \sum_{A\in n}\sum_{B\in n} \frac{1}{p_{A\to B}} \cdot \frac{(U_A - U_B)^2 C_{\mathrm{MZM}}}{2}. \tag{17}$$

Furthermore, one transmitted symbol contains $\log_2(M)$ bits leading to the following energy consumption per bit for an *IQ* modulator:

$$W_{IQ,\mathrm{bit}} = 2 \cdot W_{\mathrm{MZM}} = 2 \cdot \frac{\sum_{A\in n}\sum_{B\in n} \frac{1}{p_{A\to B}} \cdot \frac{(U_A-U_B)^2 C_{\mathrm{MZM}}}{2}}{\log_2(M)}. \tag{18}$$

For the QPSK or 4-QAM modulation format the energy per bit is given by

$$W_{IQ,\text{4-QAM,bit}} = \frac{1}{4} U_{pp-\mathrm{signal}}^2 C_{MZM}. \tag{19}$$

$$W_{IQ,\text{16-QAM,bit}} = \frac{5}{72} U_{pp-\mathrm{signal}}^2 C_{\mathrm{MZM}}. \tag{20}$$

In order to estimate the energy consumption per bit of the *IQ* modulator, the C_{MZM} capacitance was determined relying on 3-D FEM simulations (CST Microwave Studio) using the geometries as found from SEM images of the fabricated devices (C, E). With this we can then derive capacitances of 3.15 fF for device D and 7.67 fF for device C that performed QPSK operation. For device E that performed 16-QAM operation, we obtained a capacitance of 4 fF.

Applying this formula we can derive an energy consumption of 78 fJ/b (device D) and 191 fJ/b (device C) for the QPSK modulation format and a very low value of 27 fJ/b for the 16-QAM modulator when the driving voltage is $U_p = 5$ V as in our experiment.

E. Summary

The POH technology is evolving quickly. It has become a viable solution for active photonics, offering exceptionally compact devices with dimensions in the micrometer range, operation across a large optical spectrum of >100 nm, and a large electro–optical bandwidth way beyond 100 GHz. In this review, we have shown the progress from initial phase shifters to more complex *IQ* modulators that meanwhile feature ERs of >20 dB, voltage-length products of only 40 Vμm, and operation at line rates of 144 Gb/s.

Plasmonics has shown to be a viable technology not only for simple modulators but also for the most complex modulators such as *IQ* modulators. Based on this success, future large-scale implementation of plasmonics in PICs seems to become practical. To put the scaling potential in a larger context one should keep in mind that 1000 of the new plasmonic *IQ* modulators introduced here could be arranged on 1-mm^2 surface. As each of them is capable of generating 100 Gb/s, the on-chip data rate generation capability could reach 100 Tb/mm^2/s.

APPENDIX—METHODS

A. Simulations

Simulations were conducted partially by using the commercial Multiphysics FEM tool COMSOL and by using the commercial FDTD solver LUMERICAL. LUMERICAL was used to determine the PPIs' coupling

efficiency (Fig. 11) with help of full-wave 3-D simulations. COMSOL was used to solve for electrical and optical field profiles (Figs. 2 and 5) from which we derive the light–matter interaction (Figs. 6 and 7) and the achievable ER (Fig. 10). Throughout the simulations, we assumed a wavelength of 1.55 μm and the corresponding optical properties of the materials at this wavelength: $n_{\mathrm{NLO}} = 1.83$, $n_{\mathrm{SiO2}} = 1.44$, $n_{\mathrm{Si}} = 3.5$, $n_{\mathrm{SiO2}} = 1.44$, and $\varepsilon_{\mathrm{Au}} = -108.9 + 5.27j$. The Si waveguide has a height of 220 nm and a width of 450 nm. The taper angle of the Au and Si tip is 15°. The capacitance used to estimate the energy consumption of the plasmonic modulators was obtained from full-wave 3-D FEM simulations with CST Microwave Studio.

B. Enhanced Light–Matter Interaction

The light–matter interaction is quantified by the change in the effective refractive index. Based on coupled wave equations [43], one can break the light–matter interaction down to the following contributions:

$$\Delta n_{\mathrm{eff}}(U_{\mathrm{sig}}) = \Gamma \cdot n_{\mathrm{slow}} \cdot \frac{\Delta n_{\mathrm{mat}}(U_{\mathrm{sig}})}{n_{\mathrm{mat}}}. \tag{21}$$

These are the field energy interaction factor Γ, the slow down factor n_{slow}, and the relative change of the materials refractive index $\Delta n_{\mathrm{mat}}/n_{\mathrm{mat}}$. In the following, we will briefly discuss the definitions of Γ and n_{slow}. The former one is defined by

$$\Gamma \cong \frac{\epsilon_{\mathrm{mat}} \iint_{S_{\mathrm{slot}}} \left(\epsilon_0 \, E_{\mathrm{OC},x}^2\right) dS}{\iint_s \left(\epsilon_0 \frac{d\left(\epsilon(\omega)\omega\right)}{d\omega} \boldsymbol{E}_{\mathrm{OC}} \boldsymbol{E}_{\mathrm{OC}}^{+} - \mu_0 \boldsymbol{H}_{\mathrm{OC}} \boldsymbol{H}_{\mathrm{OC}}^{+}\right) dS}. \tag{22}$$

Here, the optical fields are $\boldsymbol{E}_{\mathrm{OC}}$ and $\boldsymbol{H}_{\mathrm{OC}}$. $\boldsymbol{E}^{+} = E_x\hat{\boldsymbol{x}} - E_y\hat{\boldsymbol{y}} + E_z\hat{\boldsymbol{z}}$ and $\boldsymbol{H}^{+} = -H_x\hat{\boldsymbol{x}} - H_y\hat{\boldsymbol{y}} + H_z\hat{\boldsymbol{z}}$ are the adjoint fields related to the backward propagating wave. The quotient is the ratio between the energy stored in the fields active component ($E_{\mathrm{OC},x}$) and an expression similar to the total modal energy [76]. The integral in the nominator is only evaluated over the slot's active region ($S_{\mathrm{slot}} = w \cdot h$) as the NLO material is only efficiently poled in the slot and both the RF field and the optical field are confined to this area; see Fig. 5.

The slowdown factor (n_{slow}) is given by the ratio between the modal energy (nominator) and the power flow (denominator)

$$n_{\mathrm{slow}} = c_0 \frac{\iint_S \left(\epsilon_0 \frac{d\left(\epsilon(\omega)\omega\right)}{d\omega} \boldsymbol{E}_{\mathrm{OC}} \boldsymbol{E}_{\mathrm{OC}}^{+} - \mu_0 \boldsymbol{H}_{\mathrm{OC}} \boldsymbol{H}_{\mathrm{OC}}^{+}\right) dS}{\iint_S (\boldsymbol{E}_{\mathrm{OC},t} \times \boldsymbol{H}_{\mathrm{OC},t}) \cdot \hat{\boldsymbol{z}} \, dS} \tag{23}$$

and thus, the slowdown factor can be interpreted as the refractive effective group index (energy velocity).

C. Fabrication

The devices were fabricated on a silicon-on-insulator substrate with a 220-nm high silicon device layer on top of a 3-μm-thick SiO_2 buried oxide layer. Electron-beam lithography and dry etching were used to define silicon grating couplers, multimode interference couplers, and silicon feeding waveguides. Contact electrodes and plasmonic slot waveguides were fabricated by electron beam lithography and a liftoff process applied to e-beam evaporated gold. The suspended bridges were realized with gold using a sacrificial layer. The NLO material DLD164 [61] was applied by spin coating and was poled at elevated temperatures near the glass transition temperature of the material.

D. Fabricated Devices

This review contains results obtained from various all-plasmonic Mach–Zehnder modulators and plasmonic *IQ* modulators. For a better overview, a summary of the various reported modulators' parameters is given in Table 1, where w_1 and w_2 are the width of the Mach–Zehnder's phase shifters, while l is the length of the phase shifter. h is the height of the deposited Au. In the case of the *IQ* modulators, the two MZMs are equal. ■

Acknowledgment

The authors would like to thank Prof. A. Kwiram from the University of Washington for helpful comments.

REFERENCES

[1] G. Raybon *et al.*, "Single-carrier all-ETDM 1.08-Terabit/s line rate PDM-64-QAM transmitter using a high-speed 3-bit multiplexing DAC," in *Proc. Photon. Conf.*, 2015, doi: 10.1109/IPCon.2015.7323760.

[2] B. J. Puttnam *et al.*, "2.15 Pb/s transmission using a 22 core homogeneous single-mode multi-core fiber and wideband optical comb," presented at the Eur. Conf. Opt. Commun., Valencia, Spain, 2015.

[3] R. Rodes *et al.*, "High-speed 1550 nm VCSEL data transmission link employing 25 GBd 4-PAM modulation and hard decision forward error correction," *J. Lightw. Technol.*, vol. 31, pp. 689–695, 2013.

[4] D. M. Kuchta *et al.*, "Error-free 56 Gb/s NRZ modulation of a 1530 nm VCSEL link," in *Proc. Eur. Conf. Opt. Commun.*, 2015, doi: 10.1109/ECOC.2015.7341677.

[5] G. P. Agrawal, *Lightwave Technology: Components and Devices*, New York, NY, USA: Wiley, 2004.

[6] C. Won-Jin *et al.*, "Low insertion loss and low dispersion penalty InGaAsP quantum-well high-speed electroabsorption modulator for 40-Gb/s very-short-reach, long-reach, long-haul applications," *J. Lightw. Technol.*, vol. 20, pp. 2052–2056, 2002.

[7] H. Fukano, T. Yamanaka, M. Tamura, and Y. Kondo, "Very-low-driving-voltage electroabsorption modulators operating at 40 Gb/s," *J. Lightw. Technol.*, vol. 24, pp. 2219–2224, 2006.

[8] W. Tsu-Hsiu, C. Yi-Jen, and L. Fang-Zheng, "High-speed (60 GHz) and low-voltage-driving electroabsorption modulator using two-consecutive-steps selective-undercut-wet-etching waveguide," *IEEE Photon. Technol. Lett.*, vol. 20, pp. 1261–1263, 2008.

[9] Y. Tang, J. D. Peters, and J. E. Bowers, "Over 67 GHz bandwidth hybrid silicon electroabsorption modulator with asymmetric segmented electrode for 1.3 μm transmission," *Opt. Exp.*, vol. 20, pp. 11529–11535, 2012.

[10] J. Liu *et al.*, "Waveguide-integrated, ultralow-energy GeSi electro-absorption modulators," *Nature Photon.*, vol. 2, pp. 433–437, 2008.

[11] P. Chaisakul *et al.*, "23 GHz Ge/SiGe multiple quantum well electro-absorption modulator," *Opt. Exp.*, vol. 20, pp. 3219–3224, 2012.

[12] N.-N. Feng *et al.*, "30GHz Ge electro-absorption modulator integrated with 3 μm silicon-on-insulator waveguide," *Opt. Exp.*, vol. 19, pp. 7062–7067, 2011.

[13] A. Liu *et al.*, "A high-speed silicon optical modulator based on a metal-oxide-semiconductor capacitor," *Nature*, vol. 427, pp. 615–618, 2004.

[14] L. Liao *et al.*, "High speed silicon Mach-Zehnder modulator," *Opt. Exp.*, vol. 13, pp. 3129–3135, 2005.

[15] A. Liu *et al.*, "High-speed optical modulation based on carrier depletion in a silicon waveguide," *Opt. Exp.*, vol. 15, pp. 660–668, 2007.

[16] P. Dong, L. Chen, and Y.-K. Chen, "High-speed low-voltage single-drive push-pull silicon Mach-Zehnder modulators," *Opt. Exp.*, vol. 20, pp. 6163–6169, 2012.

[17] D. Po *et al.*, "Monolithic silicon photonic integrated circuits for compact 100+Gb/s coherent optical receivers and transmitters," *IEEE J. Sel. Top. Quantum Electron.*, vol. 20, pp. 150–157, 2014.

[18] H. Xu *et al.*, "High-speed silicon modulator with band equalization," *Opt. Lett.*, vol. 39, pp. 4839–4842, 2014.

[19] E. Timurdogan *et al.*, "An ultralow power athermal silicon modulator," *Nature Commun.*, vol. 5, 2014, doi:10.1038/ncomms5008.

[20] Q. Xu, B. Schmidt, S. Pradhan, and M. Lipson, "Micrometre-scale silicon electro-optic modulator," *Nature*, vol. 435, pp. 325–327, 2005.

[21] T. Baehr-Jones *et al.*, "Nonlinear polymer-clad silicon slot waveguide modulator with a half wave voltage of 0.25 V," *Appl. Phys. Lett.*, vol. 92, 2008, Art. no. 163303.

[22] R. Ding *et al.*, "Demonstration of a low $V\pi L$ modulator with GHz bandwidth based on electro-optic polymer-clad silicon slot waveguides," *Opt. Exp.*, vol. 18, pp. 15618–15623, 2010.

[23] M. Gould *et al.*, "Silicon-polymer hybrid slot waveguide ring-resonator modulator," *Opt. Exp.*, vol. 19, pp. 3952–3961, 2011.

[24] D. Korn *et al.*, "Silicon-organic hybrid (SOH) IQ modulator using the linear electro-optic effect for transmitting 16QAM at 112 Gbit/s," *Opt. Exp.*, vol. 21, pp. 13219–13227, 2013.

[25] L. Alloatti *et al.*, "100-GHz silicon-organic hybrid modulator," *Light Sci. Appl.*, vol. 3, 2014, Art. no. e173.

[26] J. S. Schildkraut, "Long-range surface plasmon electrooptic modulator," *Appl. Opt.*, vol. 27, pp. 4587–4590, 1988.

[27] T. Nikolajsen, K. Leosson, and S. I. Bozhevolnyi, "Surface plasmon polariton based modulators and switches operating at telecom wavelengths," *Appl. Phys. Lett.*, vol. 85, pp. 5833–5835, 2004.

[28] W. Cai, J. S. White, and M. L. Brongersma, "Compact, high-speed and power-efficient electrooptic plasmonic modulators," *Nano Lett.*, vol. 9, pp. 4403–4411, 2009.

[29] H. W. Lee *et al.*, "Nanoscale conducting oxide PlasMOStor," *Nano Lett.*, vol. 14, pp. 6463–6468, 2014.

[30] A. Emboras *et al.*, "Electrically controlled plasmonic switches and modulators," *IEEE J. Sel. Top. Quantum Electron.*, vol. 21, pp. 276–283, 2015.

[31] J. A. Dionne, K. Diest, L. A. Sweatlock, and H. A. Atwater, "PlasMOStor: A metal–oxide–Si field effect plasmonic modulator," *Nano Lett.*, vol. 9, pp. 897–902, 2009.

[32] M. Pu *et al.*, "Directional coupler and nonlinear Mach-Zehnder interferometer based on metal-insulator-metal plasmonic waveguide," *Opt. Exp.*, vol. 18, pp. 21030–21037, 2010.

[33] A. Melikyan *et al.*, "Surface plasmon polariton absorption modulator," *Opt. Exp.*, vol. 19, pp. 8855–8869, 2011.

[34] J. Sorger Volker, D. L.-K. Norberto, R.-M. Ma, and X. Zhang, "Ultra-compact silicon nanophotonic modulator with broadband response," *Nanophotonics*, vol. 1, pp. 17–22, 2012.

[35] S. Zhu, G. Q. Lo, and D. L. Kwong, "Theoretical investigation of silicon MOS-type plasmonic slot waveguide based MZI modulators," *Opt. Exp.*, vol. 18, pp. 27802–27819, 2010.

[36] S. Zhu, G. Q. Lo, and D. L. Kwong, "Phase modulation in horizontal metal-insulator-silicon-insulator-metal plasmonic waveguides," *Opt. Exp.*, vol. 21, pp. 8320–8330, 2013.

[37] F. Lou, D. Dai, L. Thylen, and L. Wosinski, "Design and analysis of ultra-compact EO polymer modulators based on hybrid plasmonic microring resonators," *Opt. Exp.*, vol. 21, pp. 20041–20051, 2013.

[38] S. A. Maier *et al.*, "Plasmonics—A route to nanoscale optical devices," *Adv. Mater.*, vol. 13, pp. 1501–1505, 2001.

[39] M. Kauranen and A. V. Zayats, "Nonlinear plasmonics," *Nature Photon.*, vol. 6, pp. 737–748, 2012.

[40] D. K. Gramotnev and S. I. Bozhevolnyi, "Plasmonics beyond the diffraction limit," *Nature Photon.*, vol. 4, pp. 83–91, Feb. 2010.

[41] S. A. Maier, *Plasmonics: Fundamentals and Applications*, New York, NY, USA: Springer US, 2007.

[42] A. Melikyan *et al.*, "High-speed plasmonic phase modulators," *Nature Photon.*, vol. 8, pp. 229–233, 2014.

[43] C. Haffner *et al.*, "All-plasmonic Mach-Zehnder modulator enabling optical high-speed communication at the microscale," *Nature Photon.*, vol. 9, pp. 525–528, 2015.

[44] C. Haffner *et al.*, "Ultra-compact plasmonic IQ-modulator," in *Proc. Eur. Conf. Opt. Commun.*, 2015, doi: 10.1109/ECOC.2015.7341676.

[45] C. Hoessbacher *et al.*, "The plasmonic memristor: A latching optical switch," *Optica*, vol. 1, pp. 198–202, 2014.

[46] A. Melikyan *et al.*, "Plasmonic-organic hybrid (POH) modulators for OOK and BPSK signaling at 40 Gbit/s," *Opt. Exp.*, vol. 23, pp. 9938–9946, 2015.

[47] W. Heni *et al.*, "108 Gbit/s plasmonic Mach–Zehnder modulator with >70-GHz electrical bandwidth," *J. Lightw. Technol.*, vol. 34, no. 2, pp. 393–400, 2016.

[48] W. Heni *et al.*, "High speed plasmonic modulator array enabling dense optical interconnect solutions," *Opt. Exp.*, vol. 23, pp. 29746–29757, 2015.

[49] A. Emboras *et al.*, "Atomic scale plasmonic switch," *Nano Lett.*, vol. 16, no. 1, pp. 709–714, 2015.

[50] Y. Salamin *et al.*, "Direct conversion of free space millimeter waves to optical domain by plasmonic modulator antenna," *Nano Lett.*, vol. 15, no. 12, pp. 8342–8346, 2015.

[51] N. Kinsey, M. Ferrera,V. Shalaev, and A. Boltasseva, "Examining nanophotonics for integrated hybrid systems: A review of plasmonic interconnects and modulators using traditional and alternative materials," *J. Opt. Soc. Amer. B, Opt. Phys.*, vol. 32, pp. 121–142, 2015.

[52] S. S. Sun and L. R. Dalton, *Introduction to Organic Electronic and Optoelectronic Materials and Devices*. London, U.K.: Taylor & Francis, 2008.

[53] L. R. Dalton, P. A. Sullivan, and D. H. Bale, "Electric field poled organic electro-optic materials: State of the art and future prospects," *Chem. Rev.*, vol. 110, pp. 25–55, Oct. 2009.

[54] M. Lee *et al.*, "Broadband modulation of light by using an electro-optic polymer," *Science*, vol. 298, pp. 1401–1403, 2002.

[55] J. Leuthold *et al.*, "Silicon organic hybrid technology—A platform for practical nonlinear optics," *Proc. IEEE*, vol. 97, no. 7, pp. 1304–1316, Jul. 2009.

[56] J. Mallari *et al.*, "100 Gbps EO polymer modulator product and its characterization using a real-time digitizer," in *Proc. Opt. Fiber Commun. Conf.*, San Diego, CA, USA, 2010, Art. no. OThU2.

[57] R. W. Boyd, *Nonlinear Optics*. New York, NY, USA: Academic, 2003.

[58] T.-D. Kim *et al.*, "Binary chromophore systems in nonlinear optical dendrimers and polymers for large electrooptic activities †," *J. Phys. Chem. C*, vol. 112, pp. 8091–8098, 2008.

[59] T. Gray *et al.*, "Mesoscale dynamics and cooperativity of networking dendronized nonlinear optical molecular glasses," *Nano Lett.*, vol. 8, pp. 754–759, 2008.

[60] X.-H. Zhou *et al.*, "Supramolecular self-assembled dendritic nonlinear optical chromophores: Fine-tuning of arene-perfluoroarene interactions for ultralarge electro-optic activity and enhanced thermal stability," *Adv. Mater.*, vol. 21, pp. 1976–1981, 2009.

[61] W. W. Jin *et al.*, "Benzocyclobutene barrier layer for suppressing conductance in nonlinear optical devices during electric field poling," *Appl. Phys. Lett.*, vol. 104, Jun.16 2014, Art. no. 243304.

[62] L. Alloatti *et al.*, "100 GHz silicon-organic hybrid modulator," *Light, Sci. Appl.*, vol. 3, May 2014, Art. no. e173.

[63] S. Babar and J. H. Weaver, "Optical constants of Cu, Ag, Au revisited," *App. Opt.*, vol. 54, pp. 477–481, 2015.

[64] K. M. McPeak *et al.*, "Plasmonic films can easily be better: Rules and recipes," *ACS Photon.*, vol. 2, pp. 326–333, 2015.

[65] P. B. Johnson and R. W. Christy, "Optical constants of the noble metals," *Phys. Rev. B*, vol. 6, pp. 4370–4379, 1972.

[66] J. A. Dionne, L. A. Sweatlock, H. A. Atwater, and A. Polman, "Plasmon slot waveguides: Towards chip-scale propagation with

subwavelength-scale localization," *Phys. Rev. B*, vol. 73, 2006, Art. no. 035407.

[67] J. Tian, S. Yu,W. Yan, and M. Qiu, "Broadband high-efficiency surface-plasmon-polariton coupler with silicon-metal interface," *Appl. Phys. Lett.*, vol. 95, 2009, Art. no. 013504.

[68] W. Heni *et al.*, "High speed plasmonic modulator array enabling dense optical interconnect solutions," *Opt. Exp.*, vol. 23, pp. 29746–29757, 2015.

[69] F. Chang, K. Onohara, and T. Mizuochi, "Forward error correction for 100 G transport networks," *IEEE Commun. Mag.*, vol. 48, pp. S48–S55, 2010.

[70] P. C. Schindler *et al.*, "Monolithic GaAs electro-optic IQ modulator demonstrated at 150 Gbit/s with 64 QAM," *J. Lightw. Technol.*, vol. 32, pp. 760–765, 2014.

[71] P. Dong *et al.*, "Silicon in-phase/quadrature modulator with on-chip optical equalizer," *J. Lightw. Technol.*, vol. 33, pp. 1191–1196, 2015.

[72] M. Lauermann *et al.*, "40 GBd 16QAM signaling at 160 Gb/s in a silicon-organic hybrid modulator," *J. Lightw. Technol.*, vol. 33, pp. 1210–1216, 2015.

[73] D. Chang *et al.*, "LDPC convolutional codes using layered decoding algorithm for high speed coherent optical transmission," in *Proc. Opt. Fiber Commun. Conf.*, Los Angeles, CA, USA, 2012, Art. no. OW1H.4.

[74] S. Koeber *et al.*, "Femtojoule electro-optic modulation using a silicon-organic hybrid device," *Light, Sci. Appl.*, vol. 4, Feb. 2015, Art. no. e255.

[75] D. A. Miller, "Energy consumption in optical modulators for interconnects," *Opt. Exp.*, vol. 20, pp. A293–A308, 2012.

[76] P. Y. Chen *et al.*, "Group velocity in lossy periodic structured media," *Phys. Rev. A*, vol. 82, 2010, Art. no. 053825.

ABOUT THE AUTHORS

Christian Haffner received the M.Sc. degree in electrical engineering from the Karlsruhe Institute of Technology, Karlsruhe, Germany, in 2014, ranking first in his batch. During his study he was a scholarship holder of the German National Academic Foundation. Currently, he is working toward the Ph.D. degree at ETH Zürich, Zürich, Switzerland, in the group of Prof. J. Leuthold.

His research interest focuses on integrated plasmonics for high-speed communication.

Wolfgang Heni received the M.Sc. degree in electrical engineering and information technology from the Karlsruhe Institute of Technology, Karlsruhe, Germany, in 2013. He is currently working toward the Ph.D. degree in electrical engineering at ETH Zürich, Zürich, Switzerland, in the group of Prof. J. Leuthold.

From April 2012 to September 2012 he visited the Photonics System Group of the Tyndall National Institute, Cork, Ireland, as a research intern. His research interests include nonlinear optics, integrated plasmonics, and nanophotonic devices.

Yuriy Fedoryshyn received the M.S. degree in laser and optoelectronic technology from Lviv Polytechnic National University, Lviv, Ukraine, in 2002 and the Ph.D. degree from ETH Zürich, Zürich, Switzerland, in 2012.

He leads the micro- and nanofabrication activities at the Institute of Electromagnetic Fields, ETH Zürich. His current research is focused on plasmonic and nanophotonic devices, including modulators, switches, detectors, and light sources.

Arne Josten was born in Germany in 1986. He received the M.Sc. degree in electrical engineering and information technology from the Karlsruhe Institute of Technology (KIT), Karlsruhe, Germany, in 2013. Currently, he is working toward the Ph.D. degree at ETH Zürich, Zürich, Switzerland, in the group of Prof. J. Leuthold.

His research interests are digital signal processing for high-speed optical communication. Here a focus lies on the real-time capability of the developed schemes.

Benedikt Baeuerle was born in Germany in 1987. He received the B.Sc. and M.Sc. degrees in electrical engineering and information technology from the Karlsruhe Institute of Technology (KIT), Karlsruhe, Germany, in 2010 and 2013, respectively. Currently, he is working toward the Ph.D. degree at the Institute of Electromagnetic Fields (IEF), ETH Zürich, Zürich, Switzerland.

From March 2012 to August 2012, he visited the Photonics System Group of the Tyndall National Institute, Cork, Ireland, as a research intern. His research interests include digital signal processing, real-time processing, digital coherent transceivers, and optical transmission systems and subsystems.

Claudia Hoessbacher received the B.Sc. degree in electrical engineering and the M.Sc. degree in optics and photonics from Karlsruhe Institute of Technology, Karlsruhe, Germany, in 2010 and 2012, respectively. She is currently working toward the Ph.D. degree in the field of plasmonic and nanophotonic devices at the Institute of Electromagnetic Fields, ETH Zürich, Zürich, Switzerland.

Yannick Salamin (Student Member, IEEE) received the B.S. degree in system engineering from the University of Applied Science of Western Switzerland, Sion, Switzerland, in 2010 and the M.S. degree in electrical engineering from Zhejiang University, Hangzhou, China, in 2014. He is currently working toward the Ph.D. degree at ETH Zürich, Zürich, Switzerland.

As a B.S. student, he visited Zhejiang University for six months in 2010. From 2011 to 2014, he was with the Laboratory of Applied Research on Electromagnetic (ARE), Zhejiang University. Since 2014, he has been affiliated with the Institute of Electromagnetic Fields (IEF), ETH Zürich. His current research interests include electro-optic devices, plasmonics, microwave photonics, and metamaterials.

Mr. Salamin was the recipient of a full scholarship for postgraduate studies granted by the Ministry of Education of China (2011–2014).

Ueli Koch received the M.Sc. degree in computational science and engineering from ETH Zürich, Zürich, Switzerland, in 2013, where he is currently working toward the Ph.D. degree at the Institute of Electromagnetic Fields.

His current research interests include the numerical modeling and simulation of surface effects in plasmonic nanostructures with a particular focus on electro-optic modulation.

Nikola Đorđević received the M.Sc. degree in microsystems and nanosystems from ETH Zürich, Zürich, Switzerland, in 2014. He is currently working toward the Ph.D. degree jointly at the Institute of Electromagnetic Fields and Laboratory for Nanoelectronics, ETH Zürich.

His current research interests include integrated plasmonic and photonic devices using colloidal quantum dots.

Pol Mousel received the B.Sc. degree in electrical engineering and information technology from ETH Zürich, Zürich, Switzerland, in 2015, where he is currently working toward the M.Sc.

Romain Bonjour was born in Switzerland in 1986. He received the B.Sc. degree in industrial engineering from the University of Applied Science of Neuchatel, Switzerland, with ranking A (best possible). After his thesis on 3-D laser lithography he received the M.Sc degree (with distinction) from the "Karlsruhe School of Optics and Photonics," Karlsruhe, Germany. Currently, he is working toward the Ph.D. degree within the optical and wireless communication group at the Institute of Electromagnetic Fields, ETH Zürich, Zürich, Switzerland in 2012.

His research focus is on ultrafast microwave photonics beam steering for next-generation radio access networks.

Alexandros Emboras received his degree from the Physics department of the University of Patras and received his Ph.D degree from CEA-LETI. His thesis was focused on the design and fabrication of CMOS plasmonic modulators.

He joined ETH Zürich, Zürich, Switzerland, in November 2013 as a Senior Researcher of the Institute of Electromagnetic Fields group. Prior to that, he was a postdoctoral researcher in the optoelectronics group at Hebrew University of Jerusalem. His current research interests are the design and fabrication of novel atomic scale plasmonic devices.

David Hillerkuss, biography not available at the time of publication.

Pascal Leuchtmann received a diploma in electrical engineering and the Ph.D. degree from ETH Zürich, Zürich, Switzerland, in 1980 and 1987, respectively.

From 1980 to 1989, he was an assistant in the Electromagnetics Group (under Prof. H. Baggenstos), then scientific official in the same group. Since 1991, he has been a Lecturer at ETH and teaches courses in electromagnetics.

Dr. Leuchtmann was a member of RSI-B (2008–2011: Chair of Commission B in Germany) and a Technical Program Chair for EMC Zürich 2005 and 2009.

Delwin L. Elder received the B.S. degree in chemistry from the University of North Carolina, Chapel Hill, NC, USA, in 1994 and the Ph.D. degree from the California Institute of Technology, Pasadena, CA, USA, in 1999.

From 1999 to 2009, he was a Senior Research Chemist at Air Products and Chemicals, Inc., where his research and development projects included polymer electrolytes for lithium batteries and charge transport conducting polymers, among other things. Since 2010, he has been a Research Scientist and Lab Manager in the Chemistry Department, University of Washington, Seattle, WA, USA. His research interests include synthesis of organic nonlinear optical chromophores, device fabrication, and measurement of electro-optic coefficients, physical properties, and bulk molecular order.

Larry R. Dalton (Senior Member, IEEE) received the B.S. and M.S. degrees from the Honors College, Michigan State University, East Lansing, MI, USA, in 1965 and 1966, respectively, and the A.M. and Ph.D. degrees from Harvard University, Cambridge, MA, USA, in 1971.

He has held appointments in chemistry, electrical engineering, chemical engineering, and biochemistry, including the B. Seymour Rabinovitch Chair (University of Washington), the George B. Kauffman Professorship (University of Washington), and the Harold and the Lillian Moulton Chair (University of Southern California). He has directed or codirected the Loker Hydrocarbon Research Institute (University of Southern California), the National Science Foundation Science and Technology Center on Materials and Devices for Information Technology Research, the DARPA MORPH Program, and two DoD MURI Centers. He has coauthored over 600 publications and patents.

Dr. Dalton has been elected a Fellow of Optical Society of America (OSA), American Chemical Society (ACS), Material Research Society (MRS), The International Society for Optics and Photonics (SPIE), and American Association for the Advancement of Science (AAAS). His recent awards including a SPIE Lifetime Achievement Award, the IEEE/LEOS William Streifer Award, the American Chemical Society Award in the Chemistry of Materials, the ACS Linus Pauling Award and Medal, the ACS Richard C. Tolman Medal, and a Helmholtz International Fellow Award. He has been honored with a Festschrift Issue of the *ACS Journal of Physical Chemistry*.

Christian Hafner received the Ph.D. degree from ETH Zürich, Zürich, Switzerland, for a proposition of a new method for computational electromagnetics, the Multiple Multipole Program (MMP) in 1980. This method was also the main part of his habilitation on Computational Electromagnetics at ETH in 1987. MMP was honored by a Seymour Cray award for scientific computing in 1990.

In 1999 he was given the title of Professor at ETH and 2010-2013 he was head of the Electromagnetic Fields and Microwave Electronics Laboratory (IFH) at ETH Zürich. The focus of his current research is on the improvement, optimization, and generalization of numerical techniques of computational electromagnetics; the design and application of intelligent optimization procedures based on nature-inspired strategies; design and applications of metamaterials ranging from very low up to optical frequencies, plasmonics and optical antennas, scanning near-field microscopy, solar cells, etc. His work was published in various international journals papers, as well as in 7 books and book-software packages, which include his 2D-MMP, 3D-MMP, and MaX-1 codes. The latest MMP codes and 2D and 3D Finite Difference Time Domain (FDTD) codes and are also available in the open source package OpenMaXwell.

Juerg Leuthold (Fellow, IEEE) was born in 1966 in Switzerland. He received the Ph.D. degree in physics for work in the field of integrated optics and all-optical communications from ETH Zürich, Zürich, Switzerland.

Currently, he is the Head of the Institute of Electromagnetic Fields (IEF), ETH Zürich. From 1999 to 2004, he was affiliated with Bell Labs, Lucent Technologies, Holmdel, NJ, USA, where he performed device and system research with III/V semiconductor and silicon optical bench materials for applications in high-speed telecommunications. From 2004 to 2013, he was a full Professor at Karlsruhe Institute of Technology (KIT), Karlsruhe, Germany, where he headed the Institute of Photonics and Quantum Electronics (IPQ) and the Helmholtz Institute of Microtechnology (IMT). Since March 2013, he has been a full Professor at ETH Zürich.

Dr. Leuthold is a Fellow of the Optical Society of America. During his professorship at KIT, he was a member of the Helmholtz Association Think Tank and a member of the Heidelberg Academy of Science. From 2008 to 2011, he was chairing the Photonics Division of the Optical Society of America (OSA) and in 2010 he was the General Chair of the OSA Optics and Photonics Congress (OPC) in Karlsruhe, Germany. He has served and is serving the community as a member of the OSA Board of Directors and in many technical program committees.